

See discussions, stats, and author profiles for this publication at: <https://www.researchgate.net/publication/318874931>

Low-Temperature Solution Synthesis of Transition Metal Dichalcogenide Alloys with Tunable Optical Properties

Article in *Journal of the American Chemical Society* · August 2017

DOI: 10.1021/jacs.7b04443

CITATIONS

66

READS

859

7 authors, including:



Yifan Sun

Shanghai Jiao Tong University

26 PUBLICATIONS 2,814 CITATIONS

[SEE PROFILE](#)



Kazunori Fujisawa

Shinshu University

129 PUBLICATIONS 3,706 CITATIONS

[SEE PROFILE](#)



Zhong Lin

Pennsylvania State University

83 PUBLICATIONS 9,084 CITATIONS

[SEE PROFILE](#)



Yu Lei

Pennsylvania State University

63 PUBLICATIONS 2,183 CITATIONS

[SEE PROFILE](#)

Some of the authors of this publication are also working on these related projects:



Project

Transition Metal Oxides as Anode Materials for LIBs [View project](#)



Project

controlled fragmentation of 2D materials [View project](#)

Low-Temperature Solution Synthesis of Transition Metal Dichalcogenide Alloys with Tunable Optical Properties

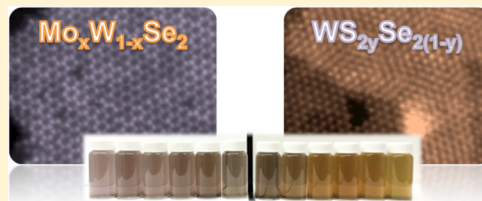
Yifan Sun,^{†,‡} Kazunori Fujisawa,^{‡,§} Zhong Lin,^{‡,||} Yu Lei,^{§,‡} Jared S. Mondschein,[†] Mauricio Terrones,^{*,†,‡,§,||} and Raymond E. Schaak^{*,†,||,‡,§,||,ID}

[†]Department of Chemistry, [‡]Department of Physics, [§]Department of Materials Science and Engineering, ^{||}Materials Research Institute, and [¶]Center for 2-Dimensional and Layered Materials, The Pennsylvania State University, University Park, Pennsylvania 16802, United States

Supporting Information

ABSTRACT: Nanostructures of layered transition metal dichalcogenide (TMD) alloys with tunable compositions are promising candidates for a broad scope of applications in electronics, optoelectronics, topological devices, and catalysis. Most TMD alloy nanostructures are synthesized as films on substrates using gas-phase methods at high temperatures. However, lower temperature solution routes present an attractive alternative with the potential for larger-scale, higher-yield syntheses of freestanding, higher surface area materials. Here, we report the direct solution synthesis of colloidal few-layer

TMD alloys, $\text{Mo}_x\text{W}_{1-x}\text{Se}_2$ and $\text{WS}_{2y}\text{Se}_{2(1-y)}$, exhibiting fully tunable metal and chalcogen compositions that span the MoSe_2 – WSe_2 and WS_2 – WSe_2 solid solutions, respectively. Chemical guidelines for achieving the targeted compounds are presented, along with comprehensive structural characterizations (X-ray diffraction, electron microscopy, Raman, and UV–visible spectroscopies). High-resolution microscopic imaging confirms the formation of TMD alloys and identifies a random distribution of the alloyed elements. Analysis of the tilt-angle dependency of the intensities associated with atomic-resolution annular dark field imaging line scans reveals the types of point vacancies present in the samples, thus providing atomic-level insights into the structures of colloidal TMD alloy nanostructures that were previously only accessible for substrate-confined films. The A excitonic transition of the TMD alloy nanostructures can be readily adjusted between 1.51 and 1.93 eV through metal and chalcogen alloying, correlating the compositional modulation to the realization of tunable optical properties.



INTRODUCTION

Layered transition metal dichalcogenides (TMDs) are of broad interest as two-dimensional (2-D) beyond-graphene materials due to their unique and diverse properties.^{1,2} Coupled by weak van der Waals interactions, each TMD layer is composed of a transition metal atom (M) covalently bonded to six chalcogen atoms (X). Hexagonal (2H) phases composed of metal–chalcogen layers stacked in a trigonal prismatic arrangement are most commonly observed, although the identities of the metal and chalcogen atoms and their coordination geometries can lead to rich polymorphism, with multiple classes of TMD structure types each having distinct properties.³ The anisotropic nature of 2-D TMD crystals facilitates the formation of both monolayer and few-layer nanosheets with unique properties that depend on their thicknesses.⁴ The group VI TMD compounds MoS_2 , WS_2 , MoSe_2 , and WSe_2 have been studied most extensively because of their narrow semiconducting band gaps that overlap well with the solar spectrum, as well as the emergence of an intrinsic indirect-to-direct band gap transition at monolayer thicknesses.⁵

Approaches such as defect engineering,⁶ strain engineering,⁷ surface functionalization,⁸ and heterostructure fabrication⁹ have been used to modify the optical properties of TMDs to realize new properties and further expand the scope of applications. A complementary approach is to form TMD alloys that can fine-

tune the physical properties by continuously modulating the elemental composition. Substitution of a parent TMD compound with different metal or chalcogen atoms alters the band structure, leading to tunable excitonic transitions between the valence band and the conduction band. Physical vapor deposition (PVD),¹⁰ chemical vapor deposition (CVD),¹¹ mechanical exfoliation of bulk TMD alloys prepared via chemical vapor transport (CVT),¹² and chalcogen exchange¹³ have been used to access TMD alloy nanosheets that are investigated for electronics,¹⁴ optoelectronics,¹⁵ catalysis,¹⁶ and topological devices.¹⁷ For example, TMD alloy monolayers exhibit tunable photoluminescence emissions,¹⁸ as well as carrier type modulation,¹⁴ and high on/off ratio in field effect transistors (FETs).¹⁹ With favorable hydrogen adsorption free energy (ΔG_H) on the edges and chemical activation on the basal planes induced by atom substitution, TMD chalcogen alloys are attractive hydrogen evolution reaction (HER) catalysts.¹⁶ Recent studies also indicate that $\text{Mo}_x\text{W}_{1-x}\text{Te}_2$ is a Type II Weyl semimetal with exotic topological properties.¹⁷

As an alternative to the synthetic methods highlighted above, solution-based routes to TMD alloy nanosheets are attractive for potentially achieving greater scalability and yield, substrate-

Received: May 1, 2017

Published: August 2, 2017

free samples with higher surface areas for catalysis, and mild reaction conditions that can lead to the formation of different phases.²⁰ However, existing solution routes to TMD alloy nanostructures require high-temperature annealing to homogeneously incorporate the alloyed elements,^{21,22} which is detrimental to nanostructure retention, surface area, and solution dispersibility, or are applicable to only a limited range of alloy compositions.^{23,24} Additionally, little is known about the atomic-level distribution of the alloyed elements in solution-synthesized TMD nanostructures.^{21–25}

Here, we report a low-temperature solution-phase approach to directly synthesize few-layer colloidal TMD alloy nanostructures. Both metal [$\text{Mo}_x\text{W}_{1-x}\text{Se}_2$] and chalcogen [$\text{WS}_{2y}\text{Se}_{2(1-y)}$] alloys across the entire solid solution ranges were obtained via isoelectronic substitution mediated by strategic selection of reagents and reaction pathways. The colloidal $\text{Mo}_x\text{W}_{1-x}\text{Se}_2$ and $\text{WS}_{2y}\text{Se}_{2(1-y)}$ alloys exhibit continuously tunable optical properties, including excitonic transitions that range from 1.51 to 1.93 eV. In addition to providing chemical guidelines for achieving complete access to the MoSe_2 – WSe_2 and WS_2 – WSe_2 solid solutions using colloidal synthesis methods, we present a detailed microscopic study that identifies the locations and distributions of the alloying elements and vacancies. Such atomic-level structural information has not been available previously for colloidal TMD nanostructures, since the few-layer nanosheets that comprise them are not flat on a substrate as they are in more traditional CVD-grown films. The approach used to obtain atomic-level microscopic insights is anticipated to be broadly applicable across a wide range of colloidal nanostructures that have buckled, crumpled, or curved components.

EXPERIMENTAL SECTION

Materials. Oleylamine (technical grade, 70%), tungsten(VI) chloride (WCl_6 , ≥99.9%, trace metal basis), diphenyl diselenide (98%), diphenyl disulfide (99%), hexamethyldisilazane (HMDS, reagent grade, ≥99%), and carbon disulfide (CS_2 , ≥99.9%, anhydrous) were purchased from Sigma-Aldrich. Molybdenum(V) chloride (MoCl_5 , 99.6%, metal basis) and oleic acid (technical grade, 90%) were purchased from Alfa Aesar. Solvents, including toluene and ethanol, were of analytical grade. All chemicals were used as received without further purification.

Synthesis of $\text{Mo}_x\text{W}_{1-x}\text{Se}_2$ Alloy Nanostructures. All reactions were carried out under an argon atmosphere using standard Schlenk techniques and workup procedures were performed in air. In the synthesis of $\text{Mo}_x\text{W}_{1-x}\text{Se}_2$, 39 mg of diphenyl diselenide (0.125 mmol) dissolved in 15 mL of oleylamine (45.6 mmol) were added to a 100 mL three-neck flask and degassed for 30 min under vacuum at 120 °C. Then, 0.5 mL of HMDS was injected into the flask after cooling to 100 °C under argon and the mixture was heated to 300 °C. Meanwhile, 0.125 mmol of MoCl_5 , WCl_6 , or a mixture of the two (Table S1) was dissolved in 1 mL of oleic acid (3.1 mmol) with sonication. The metal reagent was then injected dropwise into the hot mixture at a rate of 2 mL/h using a syringe pump. After 30 min, the injection was completed and the heating mantle was removed to allow the reaction mixture to cool to room temperature. The products were washed three times with a 1:1 toluene/ethanol mixture and kept as a powder under argon.

Synthesis of $\text{WS}_{2y}\text{Se}_{2(1-y)}$ Alloy Nanostructures. To prepare sulfur-rich chalcogen alloys with $y > 0.5$, CS_2 was used as the sulfur source, as reported previously for the synthesis of colloidal WS_2 ,²⁶ and diphenyl diselenide was used as the selenium source.²⁷ Diphenyl diselenide dissolved in 15 mL of oleylamine was added to a 100 mL three-neck flask and degassed for 30 min under vacuum at 120 °C. HMDS (0.5 mL) was then injected into the flask after cooling to 100 °C under argon and the mixture was heated to 300 °C. Meanwhile, WCl_6 (50 mg, 0.125 mmol) was dissolved in 0.3 mL of oleic acid (0.95

mmol) and mixed with 5 mL of oleylamine (15.2 mmol) in an argon-flushed septum-capped vial. Upon injection, 0.24 mL of CS_2 was introduced to the vial, forming a homogeneous solution with a temperature increase. The solution in the vial was subsequently injected dropwise into the three-neck flask at a rate of 2 mL/h using a syringe pump. Over a 30 min interval, the injection was stopped and the heating mantle was removed. After cooling down to room temperature, the products were washed three times with a 1:1 toluene/ethanol mixture, collected with centrifugation, and kept as a powder under argon. For Se-rich samples ($y < 0.5$), the synthetic approach was identical to that for $\text{Mo}_x\text{W}_{1-x}\text{Se}_2$, except diphenyl disulfide and diphenyl diselenide were dissolved together in oleylamine in the beginning and reaction time was modified. Table S2 provides detailed information about the experimental parameters. Scheme S1 in the Supporting Information summarizes the synthetic routes for both the metal and chalcogen alloys.

Characterization. Powder X-ray diffraction (XRD) patterns were collected using a Bruker-AXS D8 Advance diffractometer equipped with Cu K α radiation and a LynxEye 1-D detector. Simulated XRD patterns of WS_2 , MoSe_2 , and WSe_2 were generated using the CrystalMaker/CrystalDiffract software package. Transmission electron microscopy (TEM), high-angle annular dark-field scanning transmission electron microscopy (HAADF-STEM) images, and energy dispersive X-ray spectroscopy (EDS) data with element maps were acquired using a FEI Talos F200X operating at 200 kV. High-resolution ADF images were obtained using a FEI Titan³ G2 60/300 TEM with a spherical aberration corrector on both the probe and the image-forming lens at an accelerating voltage of 80 kV. Lower voltage was used at high resolution to decrease irradiation damage. To enhance visibility and reduce noise, all acquired high-resolution images were processed by Gaussian Blur filter using ImageJ software. STEM ADF image simulation was done by QSTEM software developed by C. Koch.²⁸ All parameters for the ADF image simulation were appropriately set according to experimental imaging condition, including acceleration voltage, spherical aberration (C_3 and C_s), convergence angle, and inner/outer angle for the ADF detector. Thermal diffuse scattering (TDS) was taken into account and tilting angle was applied by QSTEM software by rotating the sample structure. Bruker ESPRIT 2 software was applied for EDS data interpretation. Micro-Raman measurements were performed in a Renishaw inVia confocal microscope-based Raman spectrometer with 514.5 nm laser. The laser spot size using the 100 \times objective lens was approximately 1 μm . Alloy samples were dispersed in ethanol assisted by sonication and then ultraviolet-visible (UV-vis) transmittance measurements were performed using a LAMBDA 950 UV-vis/NIR spectrometer (350–1200 nm, 0.5 nm data interval).

RESULTS AND DISCUSSION

Colloidal $\text{Mo}_x\text{W}_{1-x}\text{Se}_2$ Alloy Nanostructures. The TMD alloys with variable metal element composition spanning the MoSe_2 – WSe_2 solid solution ($\text{Mo}_x\text{W}_{1-x}\text{Se}_2$) were synthesized via the dropwise injection of metal reagents (MoCl_5 , WCl_6) dissolved in oleic acid into a solution of oleylamine, HMDS, and diphenyl diselenide at 300 °C, as described in detail in the Experimental Section. MoSe_2 and WSe_2 both adopt the hexagonal 2H structure type and have closely matched lattice constants and similar electronic structures,²⁹ which helps to facilitate the formation of $\text{Mo}_x\text{W}_{1-x}\text{Se}_2$ alloys rather than a mixture of MoSe_2 and WSe_2 . Colloidal $\text{Mo}_x\text{W}_{1-x}\text{Se}_2$ nanostructures with $x = 0, 0.14, 0.35, 0.52, 0.77$, and 1 were prepared by modifying the amounts of MoCl_5 and WCl_6 dissolved in oleic acid.

Figure S1 shows powder XRD data for $\text{Mo}_x\text{W}_{1-x}\text{Se}_2$ nanostructures with $x = 0, 0.14, 0.35, 0.52, 0.77$, and 1, as well as reference patterns for bulk MoSe_2 and WSe_2 for comparison.^{30,31} It is well-known that irregular stacking of nanosheets, small domain sizes, and lattice strain induced by

defects and curvature lead to significantly broadened diffraction peaks in solution-synthesized TMD nanostructures. However, peaks corresponding to the (002), (100), (103), (105), (110), (008), (200), and (203) planes can be identified in the XRD patterns for all of the $\text{Mo}_x\text{W}_{1-x}\text{Se}_2$ nanostructures. The lattice constants for the end members are closely matched: for MoSe_2 , $a = 3.288 \text{ \AA}$ and $c = 12.931 \text{ \AA}$,³⁰ while for WSe_2 , $a = 3.282 \text{ \AA}$ and $c = 12.96 \text{ \AA}$.³¹ Therefore, the XRD patterns are nearly identical and peak positions do not shift in a significant or measurable way as x changes, which makes it difficult to distinguish between mixtures of separated MoSe_2 and WSe_2 vs the targeted $\text{Mo}_x\text{W}_{1-x}\text{Se}_2$ alloys.

To better characterize the TMD alloy nanostructures, a suite of microscopic and spectroscopic techniques were used. As is typical for solution-synthesized TMD nanostructures, the $\text{Mo}_x\text{W}_{1-x}\text{Se}_2$ nanosheets agglomerate to produce nanoflower-like morphologies,² as shown by TEM in Figure S2. As a representative example, the STEM and TEM images of $\text{Mo}_{0.35}\text{W}_{0.65}\text{Se}_2$ in Figures 1a and 1b reveal uniform nanoflowers

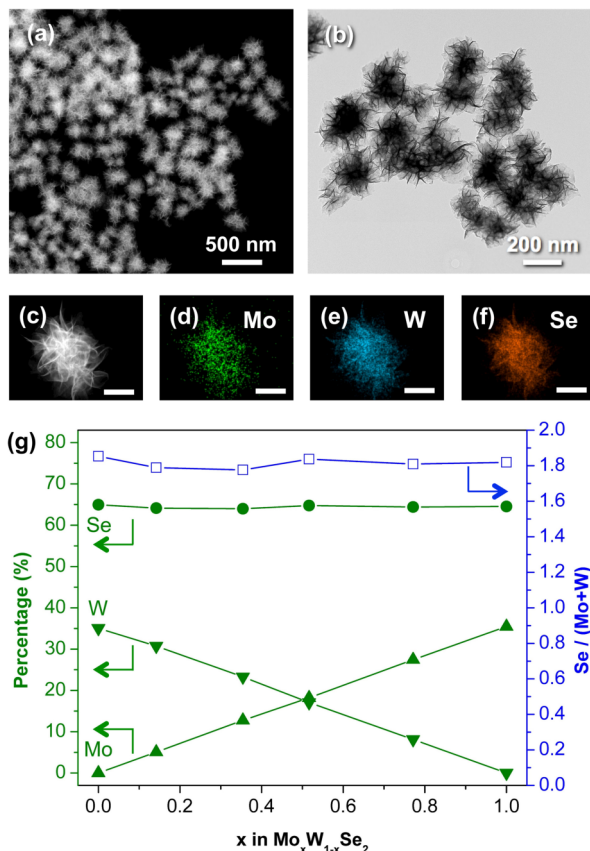


Figure 1. (a) HAADF-STEM image, (b) TEM image, and (c–f) STEM-EDS element maps (100 nm scale bars) of $\text{Mo}_{0.35}\text{W}_{0.65}\text{Se}_2$ nanostructures. (g) Plots of elemental composition (green) and metal/chalcogen ratio (blue) as a function of x in the $\text{Mo}_x\text{W}_{1-x}\text{Se}_2$ alloy nanostructures.

with diameters of approximately 200 nm. The nanoflowers are comprised of curled 2-D nanosheets that protrude from the thicker core to form a three-dimensionally structured architecture. Figure 1c–f also shows STEM-EDS mapping data for the $\text{Mo}_{0.35}\text{W}_{0.65}\text{Se}_2$ nanostructures, indicating that Mo, W, and Se are uniformly distributed throughout the nanoflowers. EDS spectra for each $\text{Mo}_x\text{W}_{1-x}\text{Se}_2$ sample, shown in

Figure S3, indicate that the Se signal is nearly constant while the Mo and W signals increase and decrease in intensity, respectively, as x increases. Figure 1g shows a plot of the relative amounts of Se, W, and Mo in each $\text{Mo}_x\text{W}_{1-x}\text{Se}_2$ sample, as derived from the EDS data in Figure S3. All samples contain ~65% Se and 35% metal (W + Mo). The Mo/W ratios vary linearly across the entire solid solution, indicating the Mo/W ratio can be readily tuned by varying the metal reagent stoichiometries. Additionally, the nearly constant chalcogen/metal ratio of approximately 1.8 implies that all of the $\text{Mo}_x\text{W}_{1-x}\text{Se}_2$ nanostructures are chalcogen-deficient. Substrate-confined TMD nanosheets synthesized using traditional gas-phase deposition routes commonly contain chalcogen defects due to intrinsic grain boundaries, atomic vacancies, or substitutional doping.⁶ Ex situ treatments, such as mechanical processing and heterolayer stacking,⁶ can also result in the formation of vacancies. For the colloidal $\text{Mo}_x\text{W}_{1-x}\text{Se}_2$ nanostructures, defects are most likely to arise from domain boundaries in the polycrystalline nanosheets,³² or chalcogen vacancies induced by Se dissolution in oleylamine at elevated temperatures.³³

Figure 2, which shows ADF-STEM images of the $\text{Mo}_{0.35}\text{W}_{0.65}\text{Se}_2$ nanoflowers, provides high-resolution, atomic-level structural and compositional information about the TMD alloys. The ADF-STEM image in Figure 2a corresponds to the edge of a $\text{Mo}_{0.35}\text{W}_{0.65}\text{Se}_2$ nanoflower; the top and left sides are closer to the center of the nanoflower, while the majority of the panel shows a terminal nanosheet that is exposed at the edge of the nanoflower. The ADF-STEM image shows that the TMD layer thickness decreases moving from the interior to the edge of the nanoflower, ultimately reaching monolayer thickness at the edges with domain sizes of 5–10 nm. While monolayer, bilayer, and trilayer domains can be differentiated by contrast, ADF-STEM has the ability to also distinguish atoms based on Z-contrast ($Z = \text{atomic number}$).³⁴ For $\text{Mo}_x\text{W}_{1-x}\text{Se}_2$, in addition to the Mo vs W site occupancies, three chalcogen configurations exist: diselenide (Se_2), monoseelenium vacancy (V_{Se}), and diselenium vacancy (V_{Se_2}). An ADF line scan was acquired from the high-resolution STEM image, as indicated by the green arrow in Figure 2b. The corresponding line scan profile, shown in Figure 2c, reveals the Mo vs W site occupancies as well as the chalcogen configurations. Simulations of the STEM-ADF intensity profile based on MoSe_2 , WSe_2 , and multiple vacancy configurations was carried out to unambiguously assign the identities of the atoms (Figure 2d and e). Based on the assumption that the dodecagonal-shaped vacancies belong to chalcogen sites, as supported from EDS quantification, simulation data, and previous reports,³⁵ the left hump of the two-peak pair was assigned as the chalcogen sublattice, and the right one was assigned as the metal sublattice. Taken together, this analysis allows identification of the Mo and W atom locations, as well as the observation of both Se_2 and V_{Se} vacancies.

A growing number of reports describe the solution synthesis of TMD nanostructures, and while the colloidal TMD nanostructures are typically crumpled, buckled, and/or aggregated, they remain of interest as potential materials for catalysis, particularly as discrete nanoflowers that expose a high density of catalytically active edge sites.³⁶ The high surface areas contributed by the 2-D layers are also of broad interest for applications in energy storage and conversion, as well as gas sensing.³⁷ It is thus important to be able to fully characterize the atomic distributions and vacancies in TMD alloy

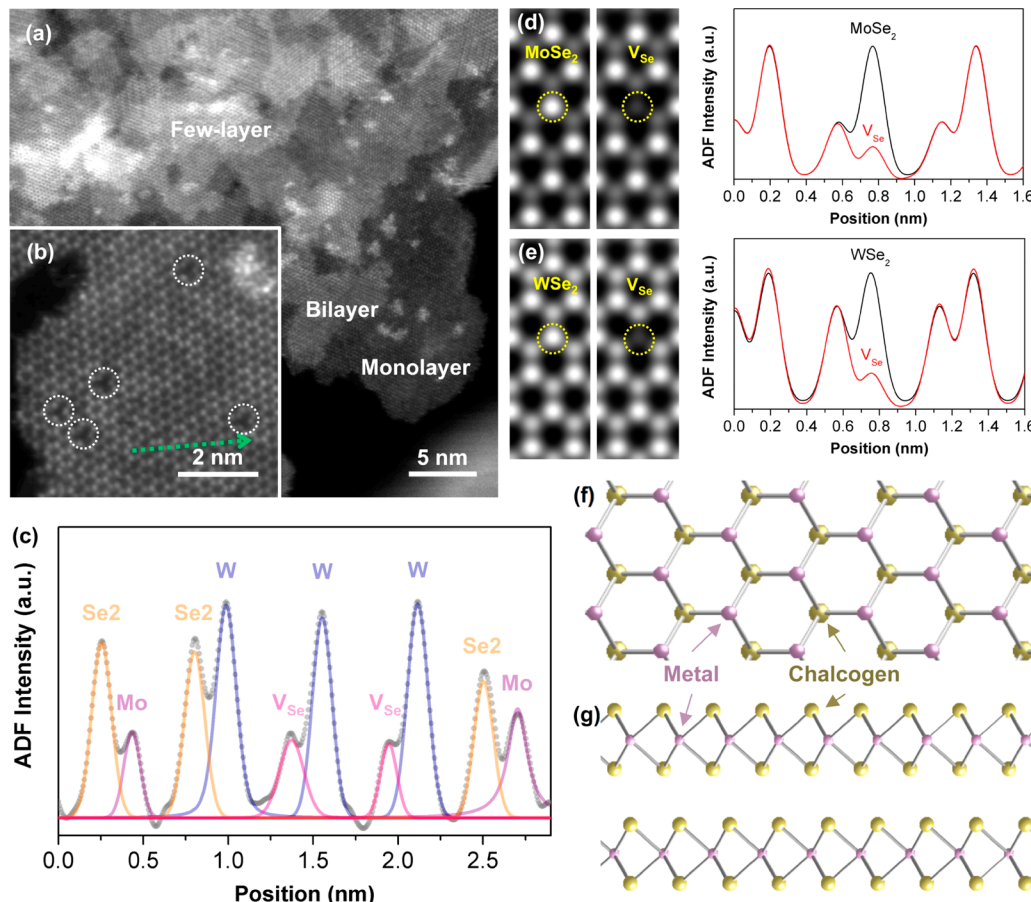


Figure 2. (a) High-resolution ADF-STEM image highlighting a region of a $\text{Mo}_{0.35}\text{W}_{0.65}\text{Se}_2$ nanostructure, showing few-layer, bilayer, and monolayer domains with overall decreasing layer thickness toward the edges. (b) Atomically resolved ADF-STEM image of $\text{Mo}_{0.35}\text{W}_{0.65}\text{Se}_2$ nanostructures, where dodecagonal-shaped chalcogen vacancies are circled. (c) Experimental ADF intensity curve (gray) corresponding to the line scan indicated by the green arrow in (b). The atoms are identified according to the simulated profiles (colored). Simulated structures of the diselenium configuration (Se_2 , black) and the monoselenium vacancy (V_{Se} , red) are shown for (d) MoSe_2 and (e) WSe_2 , along with the corresponding ADF intensity curve with 0° tilting angles. (f) Top and (g) side views of the hexagonal TMD structure, where metal (pink) and chalcogen (yellow) atoms are covalently bonded with trigonal prismatic coordination.

nanostructures, as these features are known to significantly impact properties. Taking MoS_2 as an example, both p- and n-type transfer behaviors have been identified from sulfur and molybdenum vacancies for MoS_2 , even for different regions of the same sample.³⁸ On the other hand, chemical treatment for monolayer MoS_2 induces an enhanced photoluminescence emission with near-unity quantum yield, due to the elimination of defect-mediated recombination.³⁹ Substrate-confined TMD nanosheets are flat and therefore able to be adequately characterized using microscopic techniques that rely on analysis of intensity profiles. However, TMD nanoflowers and related nanostructures that are not flat contain 2-D nanosheets that span a wide range of orientations, and as a result adopt various tilt angles relative to the imaging plane, which can significantly impact the intensity profiles.

While the STEM-ADF analysis in Figure 2 provides good agreement between the elemental assignments and compositions for the TMD metal alloy nanostructures, the relative ADF intensity ratios between the chalcogen sites and the metal sites do not match quantitatively with the simulated values. For example, simulations indicate that the Se_2 configuration should have a higher ADF intensity than W . In contrast, W appears to have a higher intensity than Se_2 in the ADF line-scan profile in Figure 2. To understand this deviation between the simulated

and observed intensities, we investigated the effect of tilt on ADF intensity. When a hexagonally structured 2H-type TMD nanosheet such as $\text{Mo}_x\text{W}_{1-x}\text{Se}_2$ is flat, the two chalcogen atoms of the Se_2 configuration are stacked in a column.⁴⁰ The ADF intensity ratio is therefore sensitive to the relative angle between the electron probe and the sample plane, because off-axis samples will be tilted relative to the electron probe, which will decrease the ADF intensity and broaden the ADF intensity profile at chalcogen positions. Figure 3a shows high-resolution ADF-STEM images for a region of a colloidal $\text{Mo}_x\text{W}_{1-x}\text{Se}_2$ nanosheet spanning tilt angles that range from 0° to 20° . Included in the imaged region are adjacent Se_2/W , $\text{V}_{\text{Se}}/\text{W}$, and $\text{V}_{\text{Se}}/\text{Se}_2$ configurations. As shown in Figure 3b, along with the corresponding plot of ADF intensity region vs tilt angle, the Se_2/W and $\text{V}_{\text{Se}}/\text{Se}_2$ configurations exhibit a strong tilt angle dependency, while the value of $\text{V}_{\text{Se}}/\text{W}$ remains nearly constant. At high tilt angles approaching 20° , the intensity from the monoselenium vacancy V_{Se} becomes close to that from the diselenium Se_2 configuration. At a tilt angle of 8° , the simulated ADF intensity ratios of Se_2/W , $\text{V}_{\text{Se}}/\text{W}$, and $\text{V}_{\text{Se}}/\text{Se}_2$ are 0.79, 0.31, and 0.40, respectively, which agree well with experimentally obtained values of 0.78, 0.35, and 0.44. This suggests that the imaged nanosheets are indeed tilted, and confirms that tilt angle analysis is important for quantitatively matching

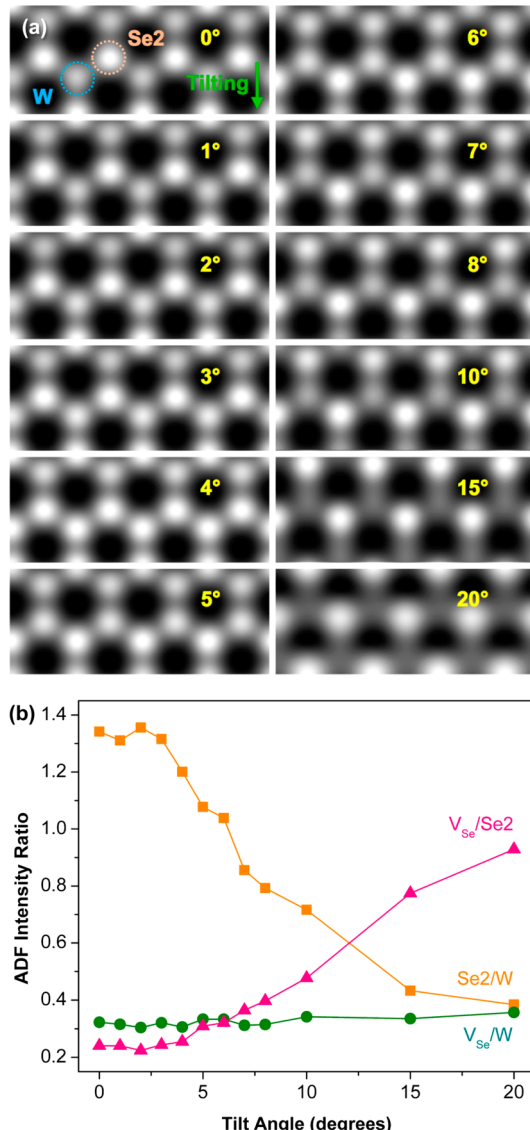


Figure 3. Effect of tilting on the STEM-ADF intensity in WSe₂ nanostructures. (a) Simulated ADF images of the structure of WSe₂ at tilting angles ranging from 0° to 20°. (b) Calculated STEM-ADF intensity ratios of V_{Se}/Se₂, Se₂/W, and V_{Se}/W at different tilting angles. Se₂ exhibits higher ADF intensity when the tilting angle is smaller than 6°, while the relationship is inverted when tilted more than 7°.

simulated and observed ADF intensity data that is used to determine the locations of the metal and chalcogen atoms in colloidal TMD nanostructures. Additional strain and curvature within the nanosheets may also impact the ADF intensity simulation, although to a lesser extent than the tilt angle. Overall, the combined analyses confirm that the colloidal TMD Mo_xW_{1-x}Se₂ nanostructures are true solid-solution alloys with atomic-level mixing of Mo and W rather than segregated phases of MoSe₂ and WSe₂.

Raman scattering spectra probes the dynamic interaction between the metal and chalcogen atoms, which provides more information about atom substitutions in low-dimensional materials.⁴¹ Figure 4 shows the Raman spectra of the Mo_xW_{1-x}Se₂ nanostructures measured with 514.5 nm laser. For MoSe₂, the out-of-plane mode A_{1g} and in-plane mode E_{2g}¹ are centered at 237.8 and 289.1 cm⁻¹, respectively, while for

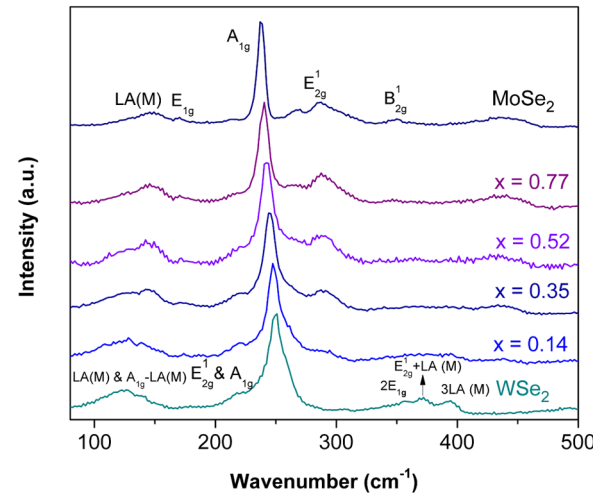


Figure 4. Raman spectra of the as-prepared Mo_xW_{1-x}Se₂ nanostructures, acquired using a 514.5 nm excitation laser. The spectra are normalized to the intensity of the A_{1g}-like peak. Raman modes are labeled based on bulk notation.

few-layer WSe₂, both modes are degenerate at around 250 cm⁻¹ to contribute to a combined A_{1g}-like peak.⁴² The A_{1g}-like mode of Mo_xW_{1-x}Se₂ shows a prominent blue shift from 237.8 to 250.0 cm⁻¹ that correlates linearly with W content (Figure S5), as interpreted with the modified random element isodisplacement (MREI) model based on effective mass and out-of-plane force constants.¹⁹ The structural evolution is also accompanied by some weak-vibration second- and higher-order modes, as evident in Figure 4. The insights gained from analysis of the Raman spectra further confirm the formation of a composition-tunable series that spans the MoSe₂–WSe₂ compositions.

Colloidal WS_{2y}Se_{2(1-y)} Alloy Nanostructures. Compared with Mo_xW_{1-x}Se₂ alloys that continuously vary the metal while keeping the chalcogen constant, the related chalcogen counterparts, WS_{2y}Se_{2(1-y)}, are more synthetically challenging. Although theoretical calculations indicate that both Mo_xW_{1-x}Se₂ and WS_{2y}Se_{2(1-y)} solid solutions are energetically favorable relative to phase-separated mixtures,⁴³ chemical issues such as precursor incompatibility,⁴⁴ chalcogen replacement,¹³ and product decomposition¹⁰ make it difficult to tune chalcogen content across the entire solid-solution range using colloidal synthesis methods. For gas-phase synthesis methods, experimental parameters including temperature gradient,¹⁸ partial vapor pressure,¹⁰ reaction time,¹³ and precursor position in the tube¹⁵ can be tailored to achieve thermodynamic or kinetic control and accomplish the atomic-level mixing of S and Se within solid-solution TMDs. Similar full-range TMD alloys have not been accessible previously as solution-synthesized colloidal nanostructures.

The successful synthesis of colloidal WS_{2y}Se_{2(1-y)} nanostructures requires careful consideration of reagent reactivity. While the MoCl₅ and WCl₆ reagents exhibit similar reactivities and therefore can be mixed together in the desired stoichiometries to obtain targeted Mo_xW_{1-x}Se₂ alloys, the available sulfur reagents evaporate and/or decompose rapidly, which substantially diminishes the utilization of sulfur during the reaction. Therefore, in contrast to the stoichiometric synthesis of Mo_xW_{1-x}Se₂, an excess of S is required to produce y-tunable WS_{2y}Se_{2(1-y)} ternary compounds. For sulfur-rich samples [WS_{2y}Se_{2(1-y)} having y = 1, 0.81, 0.70 and 0.60], diphenyl diselenide could be added directly to an existing protocol for

synthesizing colloidal WS_2 nanostructures using CS_2 as the sulfur reagent.²⁶ Increasing the amount of diphenyl diselenide beyond $\text{WS}_{1.20}\text{Se}_{0.80}$ does not result in a substantial increase of selenium incorporation, while reducing the amount of diphenyl disulfide results in amorphous products. Therefore, simple modification of the chalcogen precursor amounts cannot achieve full tunability across the $\text{WS}_2\text{--WSe}_2$ solid solution, limiting the formation of $\text{WS}_{2y}\text{Se}_{2(1-y)}$ from the WS_2 end member (i.e., sulfur-rich compositions) to a maximum of $y = 0.60$. Similar situations also occur for gas-phase CVD or PVD syntheses of TMD chalcogen alloys.^{16,45}

To access Se-rich $\text{WS}_{2y}\text{Se}_{2(1-y)}$ alloys, we began by adding the sulfur reagent to the WSe_2 end member. Diphenyl disulfide was used as the sulfur reagent instead of CS_2 due to its volatility and fast decomposition at relatively low temperatures. As shown in Table S2, the sulfur utilization is much lower than that of selenium, so excess of the sulfide reagent was used. At the same time, the typical 30 min reaction time resulted in the formation of Se-containing nanoplate impurities (Figure S6). We hypothesize that excess sulfur in solution might consume the tungsten reagent at a faster rate than selenium does, leaving unreacted selenium available for undesired side reactions. Therefore, to achieve the desired reactivity and access the targeted Se-rich $\text{WS}_{2y}\text{Se}_{2(1-y)}$ alloys, shorter reaction times were used along with tuning the S/Se reagent composition.

Figure 5a shows the XRD patterns for chalcogen alloy series. Comparing the crystal structures of end members of $\text{WS}_{2y}\text{Se}_{2(1-y)}$, the hexagonal lattice is expanded by ~4% laterally and ~5% vertically for WSe_2 vs WS_2 .³¹ The change is much larger than that for metal substitution ($\text{Mo}_x\text{W}_{1-x}\text{Se}_2$), as Se is larger than S while Mo and W are more closely matched in size. Accordingly, XRD peaks corresponding to (100), (103), (105), and (110) planes for the $\text{WS}_{2y}\text{Se}_{2(1-y)}$ samples exhibit a progressive shift to higher 2θ values as y increases. Figure S7a and b, which shows HAADF-STEM and TEM images of the $\text{WS}_{2y}\text{Se}_{2(1-y)}$ nanostructures with $y = 0.44$, reveals nanosheet aggregates having morphologies similar to the $\text{Mo}_x\text{W}_{1-x}\text{Se}_2$ samples but with less-defined and lower-density nanoflower architectures due to the shorter reaction times needed to synthesize the chalcogen alloys relative to the metal alloys. As shown in Figure S8, the average diameter of the $\text{WS}_{2y}\text{Se}_{2(1-y)}$ nanostructures decreases as the amount of incorporated sulfur increases. The STEM-EDS element maps in Figure S7c–f confirm the uniform distribution of W, S, and Se within the $\text{WS}_{1.56}\text{Se}_{0.44}$ nanostructures. The EDS spectra for all $\text{WS}_{2y}\text{Se}_{2(1-y)}$ nanostructures, shown in Figure S9 and summarized in the plot in Figure 5b, confirm the tunable S/Se composition ratio across the entire $\text{WS}_2\text{--WSe}_2$ solid solution, and indicate the chalcogen deficiency with a constant metal/chalcogen ratio (~1.8) as for the $\text{Mo}_x\text{W}_{1-x}\text{Se}_2$ metal alloys.

Similar to the data in Figure 2 for the $\text{Mo}_{0.35}\text{W}_{0.65}\text{Se}_2$ metal alloy sample, Figure 6 shows ADF-STEM images highlighting the edges of a $\text{WS}_{0.88}\text{Se}_{1.12}$ chalcogen alloy nanostructure. Monolayers, bilayers, and few-layer regions are visible, with an average domain size of ~5–10 nm (Figure 6a). At higher magnification (Figure 6b), a line scan across the monolayer region reveals information about the atom distributions in the $\text{WS}_{0.88}\text{Se}_{1.12}$ sample. Using the strategy described in detail for analysis of the $\text{Mo}_{0.35}\text{W}_{0.65}\text{Se}_2$ sample in Figure 2, we were able to identify distinct chalcogen configurations among the possibilities of diselenium (Se_2), disulfur (S_2), monosulfur plus monoselenium ($\text{S} + \text{Se}$), monoselenium vacancy (V_{Se}),

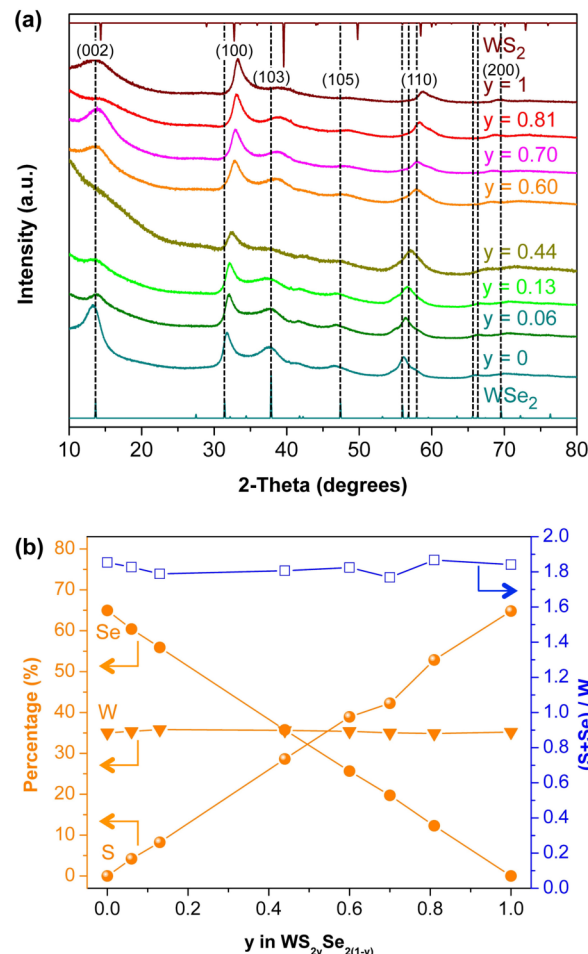


Figure 5. (a) Powder XRD patterns of $\text{WS}_{2y}\text{Se}_{2(1-y)}$ nanostructures with $y = 0, 0.06, 0.13, 0.44, 0.60, 0.70, 0.81$, and 1. Simulated diffraction patterns based on the crystal structures of bulk WS_2 and WSe_2 ³¹ are provided at top and bottom, respectively, for comparison. (b) Plots of elemental composition (orange) and metal/chalcogen ratio (blue) as a function of y in the $\text{WS}_{2y}\text{Se}_{2(1-y)}$ alloy nanostructures.

monosulfur vacancy (V_S), and double-chalcogen vacancy (V) via ADF intensity simulations (Figures 6c and 7a). These results confirm atomic-level mixing of S and Se and therefore the formation of a S:Se solid solution, and provide unprecedented insight into atomic distributions in colloidally synthesized TMD nanostructures. The different chalcogen configurations have different ADF intensities, as expected, as well as distinct characteristic peak-to-peak distances. As shown in Figure 6c, convolution of the smaller S atom results in a broad shoulder next to the W peak due to its shorter W–S bond length relative to W–Se, while the larger Se atom next to a W atom can be resolved as two distinct W and Se peaks. As for the metal alloy samples, the ADF intensity for the chalcogen alloys is also dependent on the tilt angle during imaging (Figure 7b). Accordingly, at a tilt angle of 10° , the experimentally measured ADF intensity ratios [$\text{Se}_2/\text{W} = 0.71$, $\text{S}_2/\text{W} = 0.18$, $(\text{S} + \text{Se})/\text{W} = 0.59$, and $\text{V}_{\text{Se}}/\text{W} = 0.50$] become comparable to the calculated ratios [$\text{Se}_2/\text{W} = 0.72$, $\text{S}_2/\text{W} = 0.24$, $(\text{S} + \text{Se})/\text{W} = 0.42$, and $\text{V}_{\text{Se}}/\text{W} = 0.34$].

Figure 8 shows composition-dependent Raman spectra for the $\text{WS}_{2y}\text{Se}_{2(1-y)}$ samples. WS_2 nanoflowers show the out-of-plane A_{1g} mode at 419.5 cm^{-1} , the peak contributed by the in-plane E_{2g} mode at 350.0 cm^{-1} , and the second-order 2LA(M)

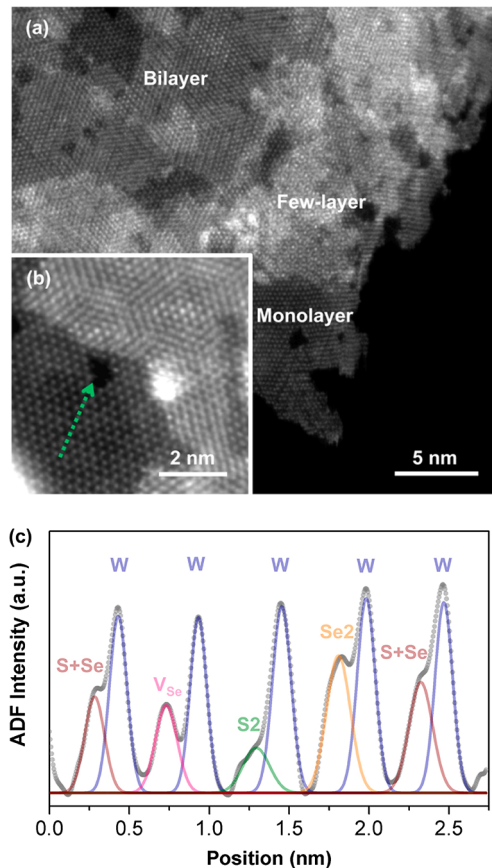


Figure 6. (a) High-resolution ADF-STEM image highlighting a region of a $\text{WS}_{0.88}\text{Se}_{1.12}$ nanostructure, showing few-layer, bilayer, and monolayer domains at the edge. (b) Atomically resolved ADF-STEM image of $\text{WS}_{2y}\text{Se}_{2(1-y)}$ nanostructures. (c) Experimental ADF intensity curve (gray) corresponding to indicated by the green arrow in (b). The atoms are identified according to the simulated profiles (colored).

mode at 356.5 cm^{-1} deconvoluted by multiplet Lorentzian fitting, as well as the first-order LA(M) mode at 174.5 cm^{-1} (Figure S11). Under excitation of a 514.5 nm laser, the Raman intensity ratio between the $2\text{LA}(M)$ mode and the A_{1g} mode increases with thinner samples as the double resonance is only active for monolayer WS_2 .⁴⁶ The fingerprint ratio in our case is around 0.7, which is between 2.2 (monolayer WS_2) and 0.47 (bulk WS_2), corroborating the few-layer structure observed by electron microscopy. The Raman peaks shift progressively upon incorporating Se. Using $\text{WS}_{0.88}\text{Se}_{1.12}$ as a representative example, the A_{1g} mode red shifts to 405.2 cm^{-1} and the peak from the E_{2g}^1 and $2\text{LA}(M)$ modes remains around 353 cm^{-1} (Figure S12). The WSe_2 feature of degenerate A_{1g} and E_{2g}^1 modes red shifts from 261.3 cm^{-1} for the $y = 0.81$ sample ($\text{WS}_{1.62}\text{Se}_{0.38}$) to 249.7 cm^{-1} for the $y = 0$ sample (WSe_2). The shift could result from tensile strain and structural distortions caused by incorporating the larger-diameter Se vs S atoms.¹⁶ Atomic disorder also contributes to the broadening of Raman peaks for alloy samples, in contrast to the sharper and more distinct peaks for the WS_2 and WSe_2 end members.

Tunable Optical Properties. UV-vis absorption spectra for all $\text{Mo}_x\text{W}_{1-x}\text{Se}_2$ and $\text{WS}_{2y}\text{Se}_{2(1-y)}$ samples dispersed in ethanol were acquired to characterize the tunable optical properties achievable through systematically modulating the metal and chalcogen compositions (Figure 9a). Figure 9b

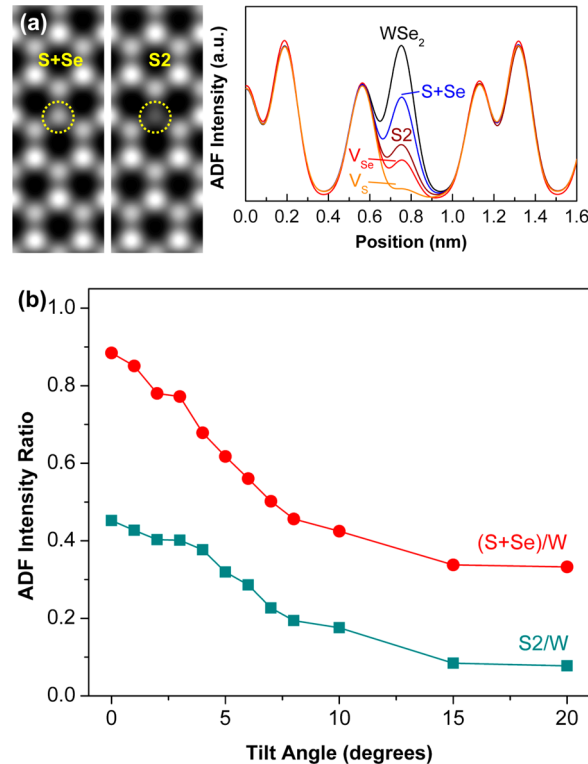


Figure 7. (a) Simulated ADF images of monosulfur plus monoselenium ($\text{S} + \text{Se}$) and disulfur ($\text{S}2$) configurations for TMD chalcogen alloys with 0° tilting angles. Calculated ADF intensity curves for diselenide ($\text{Se}2$, black), monosulfur plus monoselenium ($\text{S} + \text{Se}$, blue), disulfur ($\text{S}2$, dark red), monoselenium vacancy (V_{Se} , red), and monosulfur (V_{S} , orange) are shown on the panel to the right. The calculated ADF intensity is noticeably decreased by the presence of monoselenium vacancy (V_{Se}), which is close to that of disulfur ($\text{S}2$). (b) Calculated STEM-ADF intensity ratios of $(\text{S} + \text{Se})/\text{W}$ and $\text{S}2/\text{W}$ at different tilting angles.

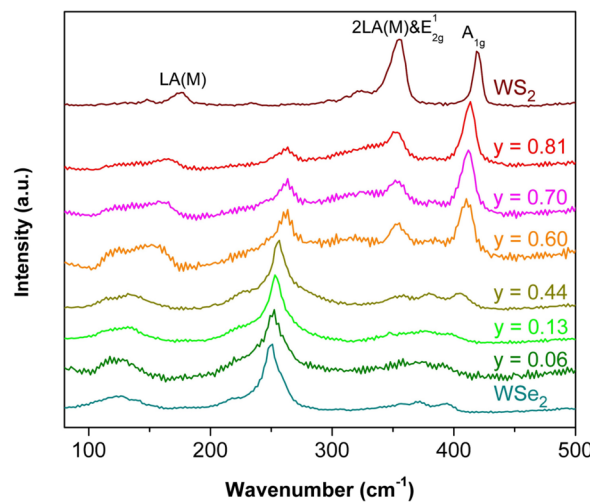


Figure 8. Raman spectra of the as-prepared $\text{WS}_{2y}\text{Se}_{2(1-y)}$ nanostructures, acquired using a 514.5 nm excitation laser. The spectra are normalized to the peak with the highest intensity for each sample. Raman modes are labeled based on bulk notation.

shows UV-vis absorption spectra for the $\text{Mo}_x\text{W}_{1-x}\text{Se}_2$ metal alloy samples. Absorption peaks are labeled according to the convention proposed by Wilson and Yoffe.⁴⁷ For MoSe_2 , A and B excitonic features arising from the valence band splitting at

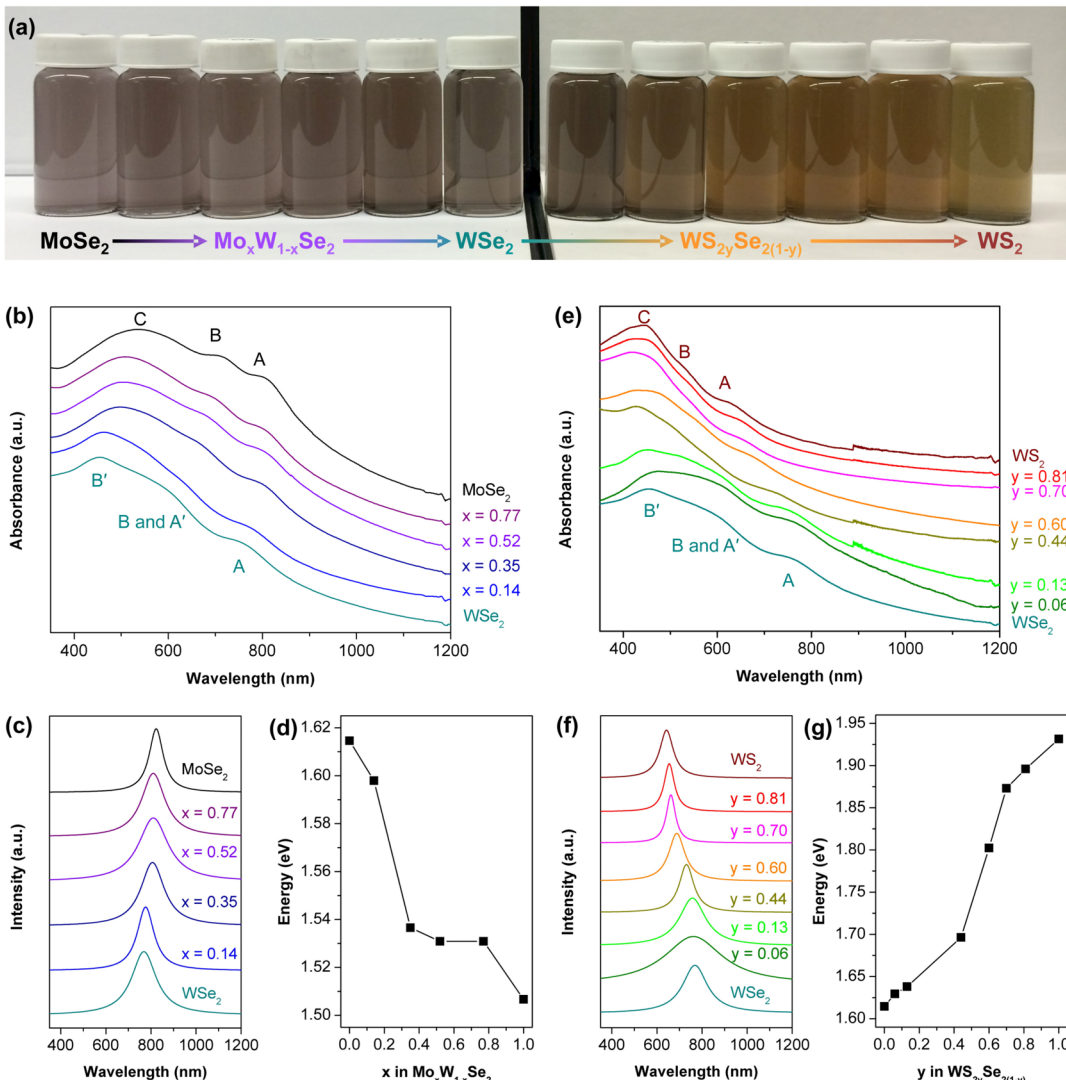


Figure 9. Tunable optical properties for colloidally synthesized TMD alloys. (a) Photograph of $\text{Mo}_x\text{W}_{1-x}\text{Se}_2$ and $\text{WS}_{2y}\text{Se}_{2(1-y)}$ samples suspended in ethanol. (b) UV–vis absorbance spectra, (c) the A excitonic peaks obtained through Lorentzian peak fitting, and (d) corresponding excitonic transition energy for $\text{Mo}_x\text{W}_{1-x}\text{Se}_2$ nanostructures. (e) UV–vis absorbance spectra, (f) the A excitonic peaks obtained through Lorentzian peak fitting, and (g) corresponding excitonic transition energy for $\text{WS}_{2y}\text{Se}_{2(1-y)}$ nanostructures. UV–vis spectra are normalized according to the highest-energy excitonic peak.

the K and K' points of the Brillouin zone appear at 823 nm (1.51 eV) and 741 nm (1.67 eV), respectively. The A excitonic transition is located at 768 nm (1.61 eV) for WSe₂, while the broad feature around 605 nm (2.05 eV) is considered as the overlap of the B and A' excitonic transitions, which could be caused by additional optical transitions and interlayer coupling for MoS₂, WS₂, MoSe₂, and WSe₂ multilayers.⁴⁸ Higher-lying interband transitions, including the C peak for MoSe₂ and the B' peak for WSe₂, require further optical measurements and band structure calculations, and are therefore out of the scope of our work.⁴⁹ Lorentzian peak fitting was utilized to determine the position of the A exciton transition. The curved background was linearly modified to partially reduce scattering effects for the samples dispersed in solution (Figure S13).^{50,51} As indicated in Figure 9c and d, the A excitonic transition ranges from 1.61 to 1.51 eV with a downward curve as the percentage of Mo in $\text{Mo}_x\text{W}_{1-x}\text{Se}_2$ increases, which could be due to uneven changes of the conduction band minimum (CBM) and the valence band maximum (VBM) through alloying.⁵² The CBM states at the K point are mainly comprised of out-of-plane d_z^2

orbitals and localized around Mo with lower energy. In contrast, the VBM states are mainly composed of in-plane d_{xy} and $d_x^2 - d_y^2$ orbitals, which introduce a uniform distribution of VBM states with wave function delocalization. As a consequence, the CBM drops rapidly as Mo is incorporated into WSe₂, while VBM decreases linearly, leading to the observed bowing toward the Mo-rich side of $\text{Mo}_x\text{W}_{1-x}\text{Se}_2$.

As displayed in Figure 9a, a gradient color change from brown to yellow is observed for the $\text{WS}_{2y}\text{Se}_{2(1-y)}$ series. The UV–vis spectra in Figure 9e reveal that the A excitonic transition exhibits a noticeable red shift with increasing Se content. The A exciton peak, which changes more significantly with composition for the chalcogen alloy system relative to the metal alloy, varies from 642 to 768 nm, corresponding to 1.93–1.61 eV, as Se incorporation increases (Figure 9f and g). As Se gradually replaces S, the bonding between the metal and the chalcogen becomes more covalent in nature, leading to broadening of the VBM d_z^2 orbital and thus a smaller energy gap at the K point.¹⁶ In addition, the gap variation of the A excitonic transition for the chalcogen alloys is more uniform

and closer to linearity compared with that for $\text{Mo}_x\text{W}_{1-x}\text{Se}_2$. The smaller bowing effect for $\text{WS}_{2y}\text{Se}_{2(1-y)}$ relative to $\text{Mo}_x\text{W}_{1-x}\text{Se}_2$ is attributed to larger lattice mismatch and chemical potential difference between diselenides and disulfides.⁴³

CONCLUSIONS

Given the broad scope of potential applications for colloidal TMD alloys with tunable compositions, it is important to identify synthetic routes capable of achieving complete metal and chalcogen solid solutions, understand how the elements are distributed throughout the nanostructures, identify the types of vacancies that are present, and correlate compositional modulation with tunable properties. Here, TMD alloy nanostructures spanning the entire MoSe_2 – WSe_2 and WS_2 – WSe_2 solid solutions have been synthesized directly in solution, without the need for additional high-temperature annealing. Chemical guidelines, complementary to existing gas-phase synthesis methods, have been identified for achieving full compositional modulation in both metal [$\text{Mo}_x\text{W}_{1-x}\text{Se}_2$] and chalcogen [$\text{WS}_{2y}\text{Se}_{2(1-y)}$] TMD alloys. Alloying was confirmed by multiple characterization techniques, and composition-dependent excitonic transitions were observed. Solution-synthesized colloidal TMD alloys, which are of interest for their high surface areas, substrate-free nature, and higher mass yields, are more challenging to characterize at the atomic level relative to substrate-confined films made by gas-phase deposition methods because of the buckled, crumpled, and semiaggregated nature of the colloidal nanostructures. Using ADF-STEM coupled with analysis of the tilt-angle dependency of the ADF intensity, important information about the atomic distributions and types of vacancies was obtained, bridging the gap between the knowledge that is already available for substrate-bound TMD alloy films and the largely unknown atomic-level details of colloidal analogues. Such fundamental insights are significant for advancing the emerging applications of TMD nanostructures in the fields of catalysis, gas sensing, and optics. Additionally, the solution synthesis capabilities demonstrated here may in the future permit the formation of ordered TMD alloys, which have been computationally predicted to have a small energetic preference to random substitutional alloys and therefore may be accessible using such low-temperature methods.^{53,54} The versatility demonstrated for tuning both the metal and chalcogen compositions suggests that Se–Te ternary TMD alloys and quaternary TMD alloys, such as $\text{Mo}_x\text{W}_{1-x}\text{S}_{2y}\text{Se}_{2(1-y)}$, may also be accessible.

ASSOCIATED CONTENT

Supporting Information

The Supporting Information is available free of charge on the ACS Publications website at DOI: [10.1021/jacs.7b04443](https://doi.org/10.1021/jacs.7b04443).

Additional synthetic details and characterization data and analyses (XRD, EDS, TEM, HAADF-STEM, Raman, and UV-vis) ([PDF](#))

AUTHOR INFORMATION

Corresponding Authors

[*mut11@psu.edu](mailto:mut11@psu.edu)

[*res20@psu.edu](mailto:res20@psu.edu)

ORCID

Raymond E. Schaak: [0000-0002-7468-8181](https://orcid.org/0000-0002-7468-8181)

Notes

The authors declare no competing financial interest.

ACKNOWLEDGMENTS

Y.S. and R.E.S. were supported by the U.S. National Science Foundation Grant No. DMR-1607135. J.S.M. was supported by funds from Penn State University. K.F., Z.L., Y.L., and M.T. acknowledge support from the U.S. Army Research Office MURI Grant W911NF-11-1-0362, the Air Force Office of Scientific Research MURI FA9550-12-1-0471, as well as the National Science Foundation for 2DARE-EFRI-1433311 and 2DARE-EFRI-1542707. M.T. and R.S. also acknowledge the Center for 2-Dimensional and Layered Materials at the Pennsylvania State University. Electron microscopy was performed at the Electron Microscopy Facility at the Materials Characterization Lab of the Penn State Materials Research Institute. We thank Jennifer Grey and Ke Wang for the assistance with TEM characterization.

REFERENCES

- (1) Chhowalla, M.; Shin, H. S.; Eda, G.; Li, L.-J.; Loh, K. P.; Zhang, H. *Nat. Chem.* **2013**, *5*, 263–275.
- (2) Lin, Z.; McCreary, A.; Briggs, N.; Subramanian, S.; Zhang, K.; Sun, Y.; Li, X.; Borys, N. J.; Yuan, H.; Fullerton-Shirey, S. K.; Chernikov, A.; Zhao, H.; McDonnell, S.; Lindenberg, A. M.; Xiao, K.; LeRoy, B. J.; Drndić, M.; Hwang, J. C. M.; Park, J.; Chhowalla, M.; Schaak, R. E.; Javey, A.; Hersam, M. C.; Robinson, J.; Terrones, M. *2D Mater.* **2016**, *3*, 042001.
- (3) Voiry, D.; Mohite, A.; Chhowalla, M. *Chem. Soc. Rev.* **2015**, *44*, 2702–2712.
- (4) Lv, R.; Robinson, J. A.; Schaak, R. E.; Sun, D.; Sun, Y.; Mallouk, T. E.; Terrones, M. *Acc. Chem. Res.* **2015**, *48*, 56–64.
- (5) Wang, Q. H.; Kalantar-Zadeh, K.; Kis, A.; Coleman, J. N.; Strano, M. S. *Nat. Nanotechnol.* **2012**, *7*, 699–712.
- (6) Lin, Z.; Carvalho, B. R.; Kahn, E.; Lv, R.; Rao, R.; Terrones, H.; Pimenta, M. A.; Terrones, M. *2D Mater.* **2016**, *3*, 022002.
- (7) Conley, H. J.; Wang, B.; Ziegler, J. I.; Haglund, R. F.; Pantelides, S. T.; Bolotin, K. I. *Nano Lett.* **2013**, *13*, 3626–3630.
- (8) Voiry, D.; Goswami, A.; Kapper, R.; Silva, C. C. C.; Kaplan, D.; Fujita, T.; Chen, M.; Asefa, T.; Chhowalla, M. *Nat. Chem.* **2015**, *7*, 45–49.
- (9) Gong, Y.; Lin, J.; Wang, X.; Shi, G.; Lei, S.; Lin, Z.; Zou, X.; Ye, G.; Vajtai, R.; Yakobson, B. I.; Terrones, H.; Terrones, M.; Tay, B. K.; Lou, J.; Pantelides, S. T.; Liu, Z.; Zhou, W.; Ajayan, P. M. *Nat. Mater.* **2014**, *13*, 1135–1142.
- (10) Feng, Q.; Mao, N.; Wu, J.; Xu, H.; Wang, C.; Zhang, J.; Xie, L. *ACS Nano* **2015**, *9*, 7450–7455.
- (11) (a) Lin, Z.; Thee, M. T.; Elías, A. L.; Feng, S.; Zhou, C.; Fujisawa, K.; Perea-López, N.; Carozo, V.; Terrones, H.; Terrones, M. *APL Mater.* **2014**, *2*, 092514. (b) Li, H.; Zhang, Q.; Duan, X.; Wu, X.; Fan, X.; Zhu, X.; Zhuang, X.; Hu, W.; Zhou, H.; Pan, A.; Duan, X. *J. Am. Chem. Soc.* **2015**, *137*, 5284–5287. (c) Li, H.; Wu, X.; Liu, H.; Zheng, B.; Zhang, Q.; Zhu, X.; Wei, Z.; Zhuang, X.; Zhou, H.; Tang, W.; Duan, X.; Pan, A. *ACS Nano* **2017**, *11*, 961–967.
- (12) Chen, Y.; Xi, J.; Dumcenco, D. O.; Liu, Z.; Suenaga, K.; Wang, D.; Shuai, Z.; Huang, Y.-S.; Xie, L. *ACS Nano* **2013**, *7*, 4610–4616.
- (13) Su, S.-H.; Hsu, Y.-Te; Chang, Y.-H.; Chiu, M.-H.; Hsu, C.-L.; Hsu, W.-T.; Chang, W.-H.; He, J.-H.; Li, L.-J. *Small* **2014**, *10*, 2589–2594.
- (14) Li, X.; Lin, M.-W.; Basile, L.; Hus, S. M.; Puretzky, A. A.; Lee, J.; Kuo, Y.-C.; Chang, L.-Y.; Wang, K.; Idrobo, J. C.; Li, A.-P.; Chen, C.-H.; Rouleau, C. M.; Geohegan, D. B.; Xiao, K. *Adv. Mater.* **2016**, *28*, 8240–8247.
- (15) Gong, Y.; Liu, Z.; Lupini, A. R.; Shi, G.; Lin, J.; Najmaei, S.; Lin, Z.; Elías, A. L.; Berkdemir, A.; You, G.; Terrones, H.; Terrones, M.; Vajtai, R.; Pantelides, S. T.; Pennycook, S. J.; Lou, J.; Zhou, W.; Ajayan, P. M. *Nano Lett.* **2014**, *14*, 442–449.

- (16) Fu, Q.; Yang, L.; Wang, W.; Han, A.; Huang, J.; Du, P.; Fan, Z.; Zhang, J.; Xiang, B. *Adv. Mater.* **2015**, *27*, 4732–4738.
- (17) Belopolski, I.; Sanchez, D. S.; Ishida, Y.; Pan, X.; Yu, P.; Xu, S.-Y.; Chang, G.; Chang, T.-R.; Zheng, H.; Alidoust, N.; Bian, G.; Neupane, M.; Huang, S.-M.; Lee, C.-C.; Song, Y.; Bu, H.; Wang, G.; Li, S.; Eda, G.; Jeng, H.-T.; Kondo, T.; Lin, H.; Liu, Z.; Song, F.; Shin, S.; Hasan, M. Z. *Nat. Commun.* **2016**, *7*, 13643.
- (18) (a) Li, H.; Duan, X.; Wu, X.; Zhuang, X.; Zhou, H.; Zhang, Q.; Zhu, X.; Hu, W.; Ren, P.; Guo, P.; Ma, L.; Fan, X.; Wang, X.; Xu, J.; Pan, A.; Duan, X. *J. Am. Chem. Soc.* **2014**, *136*, 3756–3759. (b) Wu, X.; Li, H.; Liu, H.; Zhuang, X.; Wang, X.; Fan, X.; Duan, X.; Zhu, X.; Zhang, Q.; Meixner, A. J.; Duan, X.; Pan, A. *Nanoscale* **2017**, *9*, 4707–4712.
- (19) Zhang, M.; Wu, J.; Zhu, Y.; Dumcenco, D. O.; Hong, J.; Mao, N.; Deng, S.; Chen, Y.; Yang, Y.; Jin, C.; Chaki, S. H.; Huang, Y.-S.; Zhang, J.; Xie, L. *ACS Nano* **2014**, *8*, 7130–7137.
- (20) Han, J. H.; Lee, S.; Cheon, J. *Chem. Soc. Rev.* **2013**, *42*, 2581–2591.
- (21) Meiron, O. E.; Houben, L.; Bar-Sadan, M. *RSC Adv.* **2015**, *5*, 88108–88114.
- (22) Zhang, J.; Kang, W.; Jiang, M.; You, Y.; Cao, Y.; Ng, T.-W.; Yu, D. Y. W.; Lee, C.-S.; Xu, J. *Nanoscale* **2017**, *9*, 1484–1490.
- (23) Xu, C.; Peng, S.; Tan, C.; Ang, H.; Tan, H.; Zhang, H.; Yan, Q. *J. Mater. Chem. A* **2014**, *2*, 5597–5601.
- (24) Yang, Y.; Wang, S.; Zhang, J.; Li, H.; Tang, Z.; Wang, X. *Inorg. Chem. Front.* **2015**, *2*, 931–937.
- (25) Gong, Q.; Cheng, L.; Liu, C.; Zhang, M.; Feng, Q.; Ye, H.; Zeng, M.; Xie, L.; Liu, Z.; Li, Y. *ACS Catal.* **2015**, *5*, 2213–2219.
- (26) Mahler, B.; Hoepfner, V.; Liao, K.; Ozin, G. A. *J. Am. Chem. Soc.* **2014**, *136*, 14121–14127.
- (27) Jung, W.; Lee, S.; Yoo, D.; Jeong, S.; Miró, P.; Kuc, A.; Heine, T.; Cheon, J. *J. Am. Chem. Soc.* **2015**, *137*, 7266–7269.
- (28) Koch, C. T. Ph.D. Thesis, Arizona State University, Tempe, AZ, 2002.
- (29) Huang, B.; Yoon, M.; Sumpter, B. G.; Wei, S.-H.; Liu, F. *Phys. Rev. Lett.* **2015**, *115*, 126806.
- (30) James, P. B.; Lavik, M. T. *Acta Crystallogr.* **1963**, *16*, 1183.
- (31) Schutte, W. J.; De Boer, J. L.; Jellinek, F. *J. Solid State Chem.* **1987**, *70*, 207–209.
- (32) Sun, Y.; Wang, Y.; Sun, D.; Carvalho, B. R.; Read, C. G.; Lee, C.-H.; Lin, Z.; Fujisawa, K.; Robinson, J. A.; Crespi, V. H.; Terrones, M.; Schaak, R. E. *Angew. Chem., Int. Ed.* **2016**, *55*, 2830–2834.
- (33) Sun, D.; Feng, S.; Terrones, M.; Schaak, R. E. *Chem. Mater.* **2015**, *27*, 3167–3175.
- (34) Krivanek, O. L.; Chisholm, M. F.; Nicolosi, V.; Pennycook, T. J.; Corbin, G. J.; Dellby, N.; Murfitt, M. F.; Own, C. S.; Szilagyi, Z. S.; Oxley, M. P.; Pantelides, S. T.; Pennycook, S. J. *Nature* **2010**, *464*, 571–574.
- (35) (a) Azizi, A.; Zou, X.; Ercius, P.; Zhang, Z.; Elías, A. L.; Perea-López, N.; Stone, G.; Terrones, M.; Yakobson, B. I.; Alem, N. *Nat. Commun.* **2014**, *5*, 4867. (b) Azizi, A.; Wang, Y.; Stone, G.; Elias, A. L.; Lin, Z.; Terrones, M.; Crespi, V. H.; Alem, N. *Nano Lett.* **2017**, *17*, 2802–2808.
- (36) Jaramillo, T. F.; Jørgensen, K. P.; Bonde, J.; Nielsen, J. H.; Horch, S.; Chorkendorff, I. *Science* **2007**, *317*, 100–102.
- (37) Huang, X.; Zeng, Z.; Zhang, H. *Chem. Soc. Rev.* **2013**, *42*, 1934–1946.
- (38) McDonnell, S.; Addou, R.; Buie, C.; Wallace, R. M.; Hinkle, C. L. *ACS Nano* **2014**, *8*, 2880–2888.
- (39) Amani, M.; Lien, D.-H.; Kiriya, D.; Xiao, J.; Azcatl, A.; Noh, J.; Madhvapathy, S. R.; Addou, R.; KC, S.; Dubey, M.; Cho, K.; Wallace, R. M.; Lee, S.-C.; He, J.-H.; Ager, J. W.; Zhang, X.; Yablonovitch, E.; Javey, A. *Science* **2015**, *350*, 1065–1068.
- (40) Azizi, A.; Wang, Y.; Lin, Z.; Wang, K.; Elias, A. L.; Terrones, M.; Crespi, V. H.; Alem, N. *Nano Lett.* **2016**, *16*, 6982–6987.
- (41) Zhang, X.; Qiao, X.-F.; Shi, W.; Wu, J.-B.; Jiang, D.-S.; Tan, P.-H. *Chem. Soc. Rev.* **2015**, *44*, 2757–2785.
- (42) Terrones, H.; Del Corro, E.; Feng, S.; Poumirol, J. M.; Rhodes, D.; Smirnov, D.; Pradhan, N. R.; Lin, Z.; Nguyen, M. A. T.; Elias, A. L.; Mallouk, T. E.; Balicas, L.; Pimenta, M. A.; Terrones, M. *Sci. Rep.* **2014**, *4*, 4215.
- (43) Kang, J.; Tongay, S.; Li, J.; Wu, J. *J. Appl. Phys.* **2013**, *113*, 143703.
- (44) Xie, L. M. *Nanoscale* **2015**, *7*, 18392–18401.
- (45) Feng, Q.; Zhu, Y.; Hong, J.; Zhang, M.; Duan, W.; Mao, N.; Wu, J.; Xu, H.; Dong, F.; Lin, F.; Jin, C.; Wang, C.; Zhang, J.; Xie, L. *Adv. Mater.* **2014**, *26*, 2648–2653.
- (46) Berkdemir, A.; Gutiérrez, H. R.; Botello-Méndez, A. R.; Perea-López, N.; Elías, A. L.; Chia, C.-I.; Wang, B.; Crespi, V. H.; López-Urias, F.; Charlier, J.-C.; Terrones, H.; Terrones, M. *Sci. Rep.* **2013**, *3*, 1755.
- (47) Wilson, J. A.; Yoffe, A. D. *Adv. Phys.* **1969**, *18*, 193–335.
- (48) Li, Y.; Chernikov, A.; Zhang, X.; Rigosi, A.; Hill, H. M.; van der Zande, A. M.; Chenet, D. A.; Shih, E.-M.; Hone, J.; Heinz, T. F. *Phys. Rev. B: Condens. Matter Mater. Phys.* **2014**, *90*, 205422.
- (49) Zhao, W.; Ghorannevis, Z.; Chu, L.; Toh, M.; Kloc, C.; Tan, P.-H.; Eda, G. *ACS Nano* **2013**, *7*, 791–797.
- (50) Smith, R. J.; King, P. J.; Lotya, M.; Wirtz, C.; Khan, U.; De, S.; O'Neill, A.; Duesberg, G. S.; Grunlan, J. C.; Moriarty, G.; Chen, J.; Wang, J.; Minett, A. I.; Nicolosi, V.; Coleman, J. N. *Adv. Mater.* **2011**, *23*, 3944–3948.
- (51) Fan, X.; Xu, P.; Li, Y. C.; Zhou, D.; Sun, Y.; Nguyen, M. A. T.; Terrones, M.; Mallouk, T. E. *J. Am. Chem. Soc.* **2016**, *138*, 5143–5149.
- (52) Tongay, S.; Narang, D. S.; Kang, J.; Fan, W.; Ko, C.; Luce, A. V.; Wang, K. X.; Suh, J.; Patel, K. D.; Pathak, V. M.; Li, J.; Wu, J. *Appl. Phys. Lett.* **2014**, *104*, 012101.
- (53) Gan, L.-Y.; Zhang, Q.; Zhao, Y.-J.; Cheng, Y.; Schwingenschlögl, U. *Sci. Rep.* **2014**, *4*, 6691.
- (54) Tan, T. L.; Ng, M.-F.; Eda, G. *J. Phys. Chem. C* **2016**, *120*, 2501–2508.